Filaments in simulations of molecular cloud formation

Gilberto C. Gómez & Enrique Vázquez-Semadeni
Centro de Radioastronomía y Astrofísica, Universidad Nacional Autónoma de México, Campus Morelia
Apartado Postal 3-72, 58090, Morelia, Michoacán, México

ABSTRACT

We report on the filaments that develop self-consistently in a new numerical simulation of cloud formation by colliding flows. As in previous studies, the forming cloud begins to undergo gravitational collapse because it rapidly acquires a mass much larger than the average Jeans mass. Thus, the collapse is hierarchical in nature, proceeding along its shortest dimension first. This naturally produces filaments in cloud, and clumps within the filaments. The filaments are not in equilibrium at any time, but instead are long-lived flow features, through which the gas flows from the cloud to the clumps. The filaments are long-lived because they accrete from their environment while simultaneously accreting onto the clumps within them; they are essentially the locus where the flow changes from accreting in two dimensions to accreting in one dimension. Moreover, the clumps also exhibit a hierarchical nature: the gas in a filament flows onto a main, central clump, but other, smaller-scale clumps form along the infalling gas. Correspondingly, the velocity along the filament exhibits a hierarchy of jumps at the locations of the clumps. Two prominent filaments in the simulation have lengths $\sim 15\,$pc, and masses $\sim 600 M_\odot$ above density $n \sim 10^3\,\mathrm{cm}^{-3}$ ($\sim 2\times10^3 M_\odot$ at $n > 50\,\mathrm{cm}^{-3}$). The density profile exhibits a central flattened core of size $\sim 0.3\,$pc and an envelope that decays as $r^{-2.5}$, in reasonable agreement with observations. Accretion onto the filament reaches a maximum linear density rate of $\sim 30 M_\odot\,\mathrm{Myr}^{-1}\,\mathrm{pc}^{-1}$.

Subject headings: ISM: clouds — ISM: evolution — Stars: formation

1. Introduction

Filamentary structure is ubiquitous in molecular clouds, both actively star forming and quiescent (e.g., Bally et al. 1987; Feitzinger et al. 1987; Gutermuth et al. 2008; Myers 2009; Juvela et al. 2009; André et al. 2010; Henning et al. 2010; Men'shchikov et al. 2010; Molinari et al. 2010; Schneider et al. 2010; Arzoumanian et al. 2011; Kirk et al. 2013). Moreover, these works have shown that, regardless of whether the filaments are actively forming stars or not, they often contain dense clumps and cores, which may or may not harbor young stellar objects. If not, the cores are labeled "prestellar".

Numerous physical mechanisms have been advocated for the formation of the filaments, such as the gravitational instability of a flattened isothermal cloud, with and without magnetic fields (e.g., Larson 1985; Miyama et al. 1987; Gehman et al. 1996; Nagai et al. 1998; Curry 2000; Balsara et al. 2001); supersonic MHD isothermal turbulence (e.g., Padoan et al. 2001; Goldsmith et al. 2008); and turbulence in thermally unstable gas (e.g., Klein & Woods 1998; Vázquez-Semadeni et al. 2006; Walder & Folini 2000; Pavlovski et al. 2002)

This means that, although the interstellar medium is highly turbulent, the dynamics and structure of star-forming molecular clouds may actually be dominated by gravity. This should not be surprising, since examples of gravitationally-dominated filamentary sctructures are well known, like the large-scale structure of the local universe. In the cosmological case, the filamentary structures are hardly in equilibrium. On the contrary, the filaments feed material to the clusters sitting within them and performing a definitive influence on the evolution of the galaxies in the clusters. Since observations of nearby molecular clouds show a sim-

ilar hub-filament structure (Myers 2009), as well as recent simulations of molecular cloud formation (e.g., Vázquez-Semadeni et al. 2007; Vázquez-Semadeni et al. 2011; Heitsch et al. 2009; Naranjo-Romero et al. 2012) it is easy to infer that the environment might have an influence in the evolution of pre-stellar cores (see also Gómez et al. 2007).

That the structure in molecular clouds resembles that of the dark matter in cosmological simulations may seem strange at first, since, after all, dark matter is believed to be a pressureless medium, while molecular gas is known to behave approximately isothermally, and to be at much larger thermal pressures than the general ISM. However, more careful examination shows that there is really no conflict between these facts.

When a cloud forms by means of a large-scale, coherent compression in the ISM, driven, for example, by kpc-scale instabilities (e.g., Elmegreen 1987; Kim et al. 2002), or simply by the generic turbulence in the medium (e.g., Heiles & Troland 2003), it may start out containing a large number of Jeans masses, and thus engage in global gravitational collapse (Vázquez-Semadeni et al. 2007). However, because it is internally turbulent (Koyama & Inutsuka 2002; Audit & Hennebelle 2005; Heitsch et al. 2005; Vázquez-Semadeni et al. 2006), it contains nonlinear density fluctuations that may collapse on their own in shorter tiemscales than that of the whole cloud, causing a regime of hierarchical gravitational fragmentation (i.e., of collapses within collapses; Vázquez-Semadeni et al. 2009), similar to the regime originally proposal of Hoyle (1953), except that it is seeded with nonlinear density fluctuations (see, e.g., the review by Vazquez-Semadeni 2012). As noted by Hoyle (1953), if the collapse is nearly isothermal, then the Jeans mass decreases as the cloud collapses, and thus the cloud contains an ever increasing number of Jeans masses. This implies that the collapsing cloud behaves as a pressure-free flow. The thermal pressure does indeed increase during the collapse, but it is always lagging behind the gravitational energy density, and by an ever-larger margin. In this way, the collapse of a turbulent, isothermal cloud behaves similarly to the pressureless dark matter fluid. In turn, it is well known that, under pressure-free conditions, the collapse of a spheroid proceeds by enhancing its eccentricity, effectively collapsing first along its shortest dimension, and thus proceeding to form first sheets and then filaments (Lin et al. 1965).

In this paper, we present a new, high-resolution numerical simulation of dense cloud formation by colliding flows, and report the physical conditions of the filaments that develop in this simulation by gravitational contraction. The plan of the paper is as follows: in Sec. 2 we present the numerical simulation, to then discuss its global evolution in Sec. 3. Next, in Sec. 4 we report the physical properties and conditions in one fiducial filament that develops in the simulation. Finally, in Sec. 5, we present a summary and our conclusions.

2. Numerical model

The simulation used in this study is similar to the simulation L256Δv0.17 discussed in Vázquez-Semadeni et al. (2007, hereafter Paper I), although performed at a significantly higher resolution ($296^3 \approx 2.6 \times 10^7$ SPH particles *versus* $148^3 \approx 3.2 \times 10^6$), and peroformed with the GADGET-2 code, while in Paper I the code GADGET was used. While the general behavior of the simulation is the same, the higher resolution causes some differences in the details of the evolution, which we describe below. We refer the reader to Paper I for specific details of the setup and a description of the more general behavior.

The simulation was performed in a box of 256 pc per side, initially filled with warm gas of uniform density (1 cm^{-3}) and temperature ($T = 5206$ K). Two cylindrical regions within this box were set to collide within this box, with initial velocities $v_{\rm inf}$ ($= 9.2\,{\rm km\ s^{-1}} = 1.22 c_s$, where c_s is the adiabatic sound speed), and $-v_{\rm inf}$, so that they collide at the central (y, z) plane of the box. The dimensions of the cylinders were $l_{\rm inf} = 112$ pc and $r_{\rm inf} = 32$ pc. In addition to these flows, small-amplitude turbulent motions were added to the gas, in order to break the symmetry of the setup and allow the development of instabilities in the dense layer formed by the collision (the cloud). As in Paper I, the code was modified to model the formation of sink particles. Specifically, in order to prevent the timestep from becoming arbitrarily small when a certain region of the flow undergoes gravitational collapse, once a region becomes

denser than a certain threshold $n_{\rm sf}$, it undergoes a number of tests to determine whether it is collapsing. If the tests are passed, then the mass in the region is removed from the gas phase and a "sink particle" is created, which inherits the total mass and momentum of the removed SPH particles (Bate et al. 1995; Jappsen et al. 2005; Federrath et al. 2010). In turn, the sink particle itself may continue to accrete mass from the gas phase. In the present simulation, we have taken $n_{\rm sf} = 3.2 \times 10^6\,{\rm cm}^{-3}$. In addition, we also implemented the radiative heating and cooling function used in Paper I, which in turn was taken from Koyama & Inutsuka (2002).

The collision of the flows in the center of the box induces a phase transition in the flow from diffuse-warm to cold-dense gas, producing a dense layer of cold gas that grows in mass over time (Vázquez-Semadeni et al. 2006). The ram pressure-confined dense layer is subject to bending-mode and hydrodynamical instabilities, causing the development of moderately supersonic turbulence within it (Vishniac 1994; Walder & Folini 2000; Heitsch et al. 2005, 2006; Vázquez-Semadeni et al. 2006), which in turn produces nonlinear density fluctuations. Moreover, the dense layer continues to accrete gas from the original inflows, thus increasing its mass. Eventually, as was shown in Paper I, the layer at large becomes gravitationally unstable and begins to contract. Some time later, before the global contraction is completed, the local density fluctuations also become unstable due to the decrease of the average Jeans mass, and begin to collapse themselves. Because they are nonlinearly overdense with respect to the global cloud average, they have shorter free-fall times than that of the cloud at large, completing their collapse before the whole cloud does.

3. Global evolution

In the simulation presented in Paper I, most of the early star formation occured in a high density ring that formed at the periphery of the surface where the inflowing cylinders collide. Instead, in the higher-resolution run presented here, the lower numerical viscosity allows the gas to squirt out more freely from the colliding region, so that the high density ring does not form (see fig. 1). This has two implications. First, while in the run from Paper I all the initial local collapses occurred in the peripheral ring, in the present simulation they occur throughout the dense layer. Second, while in Paper I the ring itself quicly began contracting and falling onto the center of the dense layer, here, in the absence of such a ring, both the local and global collapses are less focused, and thus take longer to develop. So, while sink formation started at $t \approx 17\,{\rm Myr}$ in Paper I, here it begins at $t \approx 20\,{\rm Myr}$.

Also, the global collapse is less coherent. While in Paper I the time at which the ring reaches the simulation center is very well defined, signaling the culmination of the large-scale collapse, here the dense layer fragments into filaments, which then form clumps, onto which the rest of the filament continues to accrete. This is understood in terms of the fact that the collapse timescale for a long filament of aspect ratio A is longer than that of a roughly spherical clump of the same volume density by a factor between $\sim A^{1/2}$ and $\sim A$, depending on whether the collapse is homologous or proceeds outside-in (Toalá et al. 2012; Pon et al. 2012). Only later, the entire filament-clump system falls into the large-scale potential well at the center of the simulation.

The fact that the usage of higher resolution (and perhaps also the different version of the code) produce a different morphological pattern is a reflection of the chaotic nature of the system, which exhibits sensitivity to initial conditions (i.e., arbitrarily nearby initial conditions end up producing very different states after finite evolution times. However, the differences occur only at the level of morphological detail, and with timing differences at the 10% level. Statistically, the two simulations behave in a similar manner, developing local collapses that culminate earlier than the global collapse.

It is important to remark that the collision of WNM currents, aided by thermal instability, initially forms a planar structure, or sheet-like cloud, which rapidly becomes Jeans-unstable and breaks into filamentary structures. In parallel, the sheet keeps accreating material from the inflows, implying that the amount of gas that has undergone the phase transition into CNM (the cloud's mass) increases in time. In a similar way, once formed, the filaments accrete mass from the

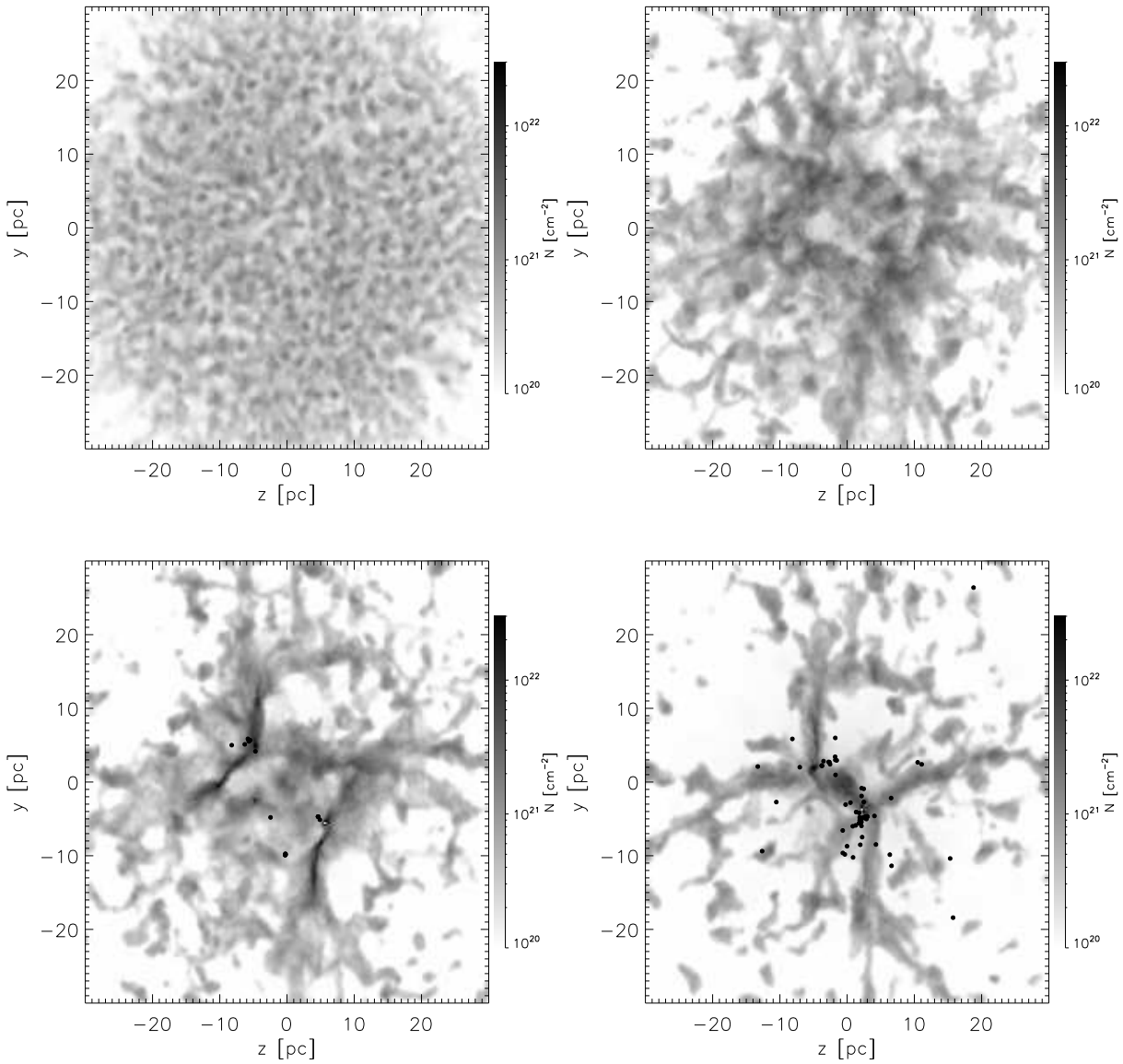

Fig. 1.— Face-on view of the central 60 pc of the simulation along the axis of the colliding flows. Grayscale represents the gas column density integrated over ±15 pc around the contact point of the initial flows, at the center of the simulation box. Times shown correspond to $t = 9.30, 17.93, 23.91$ and 30.41 Myr from the onset of the simulation. Dots indicate the positions of the sink particles in the range depicted. Coordinates are measured from the center of the simulation box.

larger planar structure, increasing their mass until they become gravitationally unstable; the filaments then collapse as a whole. But, in turn, the filaments fragment into a number of clumps because they have a longer free-fall time than any roughly spherical, Jeans-unstable fluctuation within them (Toalá et al. 2012; Pon et al. 2012). Thus, the clumps within the filaments increase their own density and develop a density contrast with respect to their parent filament. Material from the filament continues to "rain down" (accrete) onto the clumps, while continuing to be fed by the accretion flow from the sheetlike cloud.

The whole system thus constitutes a mass cascade from the largest to the smallest scales in the cloud, similar to that envisioned by Field et al. (2008), except that those authors proposed a process in which the energy released by the collapse at each scale produces random, quasi-isotropic motions at a smaller scale (see their Sec. 3). Instead, what we observe in our simulation is a continuous gravitational collapse all the way down to the protostar scale, as observed, for example, by Galván-Madrid et al. (2009), Schneider et al. (2010), and Csengeri et al. (2011). Also, a distinctive feature of this cascade is that the structures at different scales have different morphologies: from sheets to filaments, and from filaments to clumps.

A crucial feature of these structures is that *none of them is in equilibrium.* Instead, they represent a continuous flow towards the troughs of the gravitational potential, at both local and global scales, giving rise to a regime of collapses within collapses, or *hierarchical gravitational fragmentation* (Vázquez-Semadeni et al. 2009). Structures are actually *features of the flow* that persist because they continuously being fed by the accretion flow. One very important kind of such features are the filaments, which recently have received much observational attention. In Fig. 1 we show four snapshots of the simulation viewed face-on, showing the formation of the filaments and then their merging to form a final dense collapse center. In the remainder of the paper, we now discuss the physical properties of the filaments that develop in our simulation.

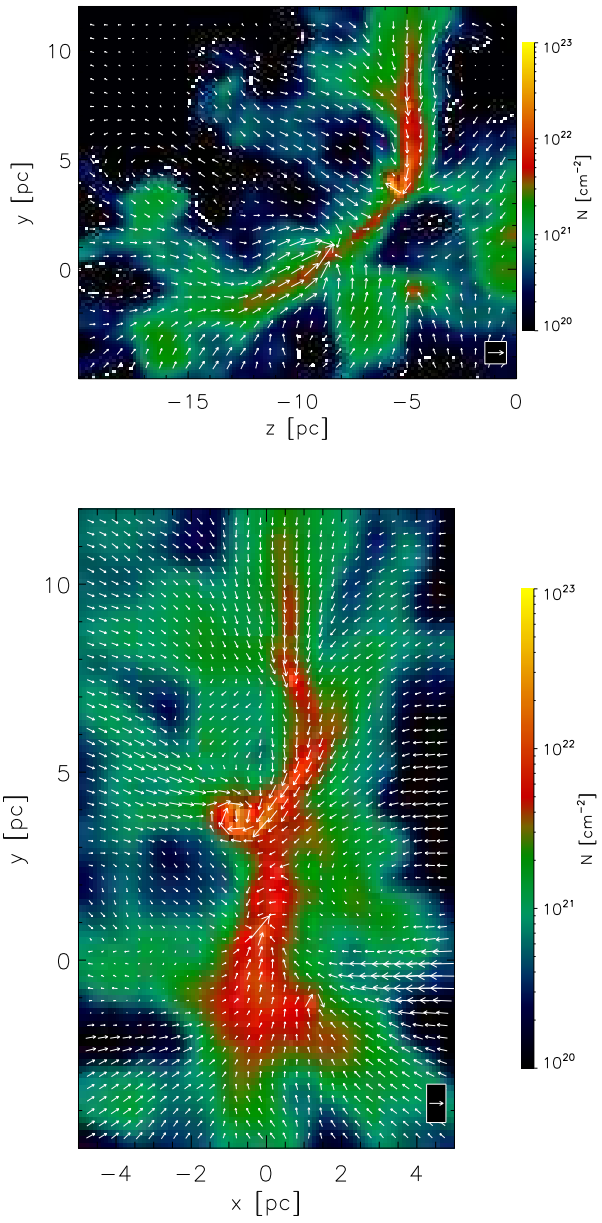

Fig. 2.— Filament 1 at 26.56 Myr into the simulation. Colors show the column density of the gas integrated over the range $|x| < 5\,\mathrm{pc}$ for the top panel, and $-20\,\mathrm{pc} < z < 0$ for the bottom panel. Coordinates are measured with respect to the center of the simulation box. The arrows show the density-weighted projected velocity field, with the arrow in the lower right representing 2 km s^{-1}. See the electronic edition of the Journal for a color version of this figure.

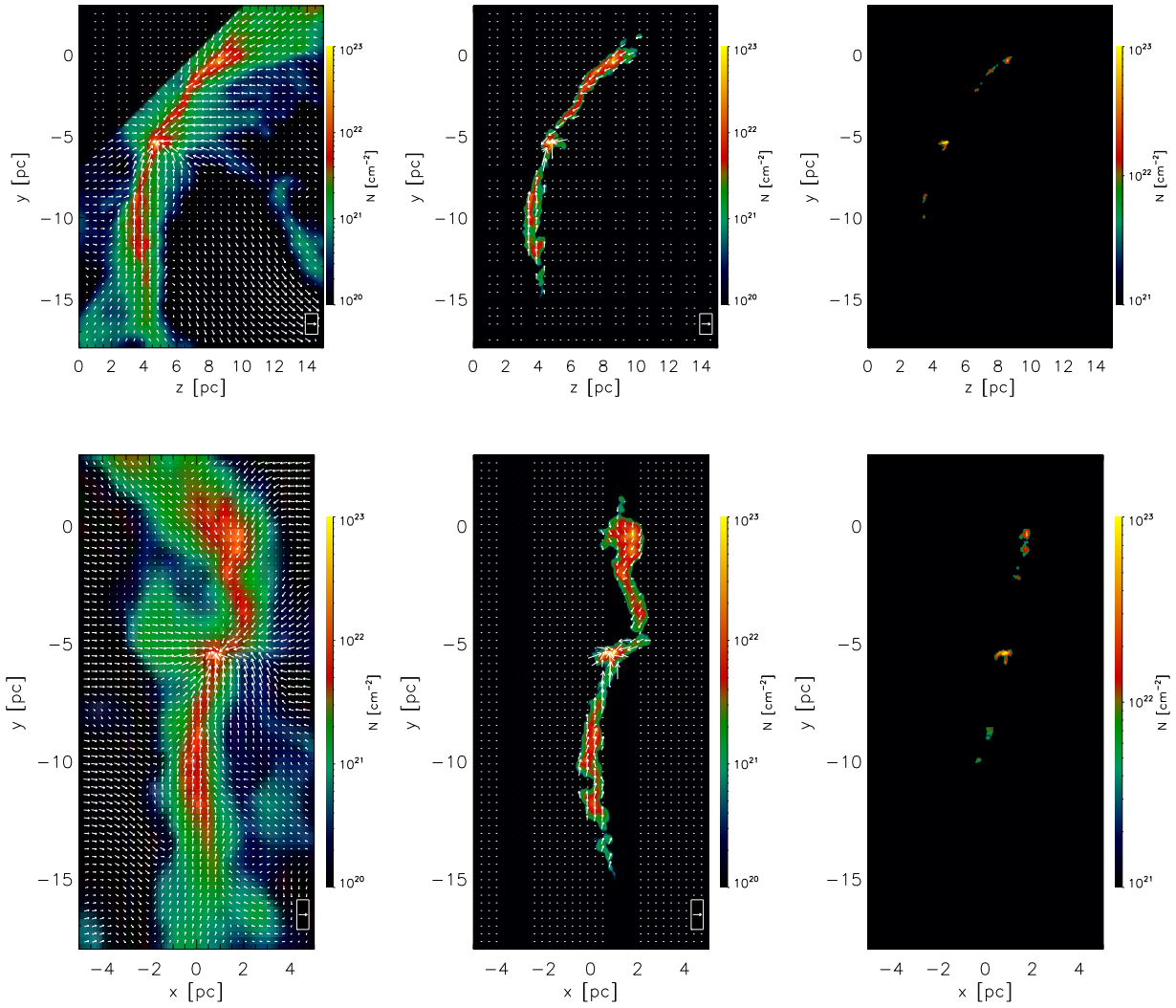

Fig. 3.— Filament 2 at 26.56 Myr into the simulation, integrated in the ranges $|x| < 5\,\mathrm{pc}$ for the top row, and $0 < z < 15\,\mathrm{pc}$ for the bottom row. Left column shows the total column density, while the middle column shows column density for gas with $n > 10^3\,\mathrm{cm}^{-3}$, and $n > 10^4\,\mathrm{cm}^{-3}$ in the right column. In all cases, the arrows show the density-weighted projected velocity, with the arrow in the lower right representing $2\,\mathrm{km\ s}^{-1}$. The region $z - y \geq 7\,\mathrm{pc}$ is suppressed to avoid a separate condensation unrelated to the filament of interest. See the electronic edition of the Journal for a color version of this figure. The bottom row of this figure is also available as mpeg animations in the electronic edition of the *Astrophysical Journal*.

4. Dense filaments

4.1. Identification

Two major filaments are readily noticeable in the lower left panel of Fig. 1 ($t = 17.9$ Myr); we shall refer to the one centered at $(z, y) \approx (-7.6, 2.8)$ pc as "Filament 1", and to the one centered at $(z, y) \approx (6.8, -5.3)$ pc as "Filament 2". Figures 2 and 3 show column density images of Filaments 1 and 2, respectively, in both the (z, y) and the (x, y) planes. The coordinates shown in the axes are measured with respect to the center of the simulation box.

When only gas with density $n > 10^3\,\mathrm{cm}^{-3}$ is considered, Filament 1 has a mass $\sim 560 M_\odot$ ($\sim 2.4 \times 10^3 M_\odot$ if we consider gas with $n > 50\,\mathrm{cm}^{-3}$), and is ~ 12 pc long and ~ 1 pc wide. Its mean density ($5.18 \times 10^4\,\mathrm{cm}^{-3}$) and aspect ratio imply an approximate free-fall time of 0.72 Myr (Toalá et al. 2012). Filament 2 has a mass $\sim 680 M_\odot$ when defined by a threshold $n > 10^3\,\mathrm{cm}^{-3}$ ($\sim 2 \times 10^3 M_\odot$ when gas with $n > 50\,\mathrm{cm}^{-3}$ is considered), has an approximate length of ~ 15 pc, and a width ~ 1 pc; its mean density ($7.88 \times 10^4\,\mathrm{cm}^{-3}$) and aspect ratio imply an approximate free-fall time of 0.66 Myr.

4.2. Local gravitational collapse

As discussed in §3, the filaments soon develop dense cores. By the time shown in Figs. 2 and 3, some of those collapse centers have already created sink particles (35, totaling $2.24 \times 10^3 M_\odot$). Thus, each of the individual structures formed from the original collision of WNM currents acts as a channel that funnels mass from the parent to the child structures. Moreover, as time goes on, the scale of the filament-clump system grows, involving increasing amounts of mass and correspondingly larger spatial scales. For example, in the bottom-right panel of Fig. 1 a large accreting clump is seen to have formed at the center of the frame, with large-scale filaments accreting onto it.

The picture described above may be verified by exploring the velocity field along the filaments. In order to do this, we have calculated the column density along lines of sight (LOSs) approximately perpendicular to the filaments. That is, the LOSs are at angles of $-50°$ and $-20°$ on the z-y plane of Figs. 2 and 3, respectively). The resulting col-

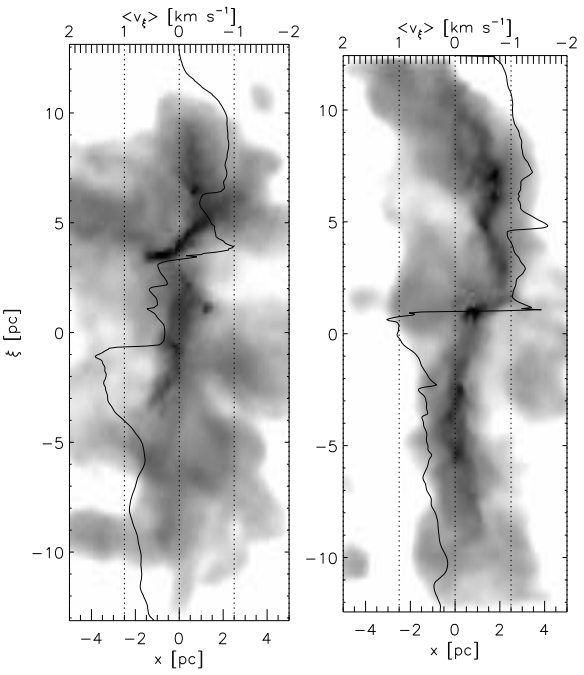

Fig. 4.— Projections perpendicular to the filaments. The grayscale shows the column density along a line of slope $-50°$ in the z-y plane (*top panel*) of Fig. 2 for Filament 1 (*left*), and $-20°$ in the z-y plane (*top panel*) of Fig. 3 for Filament 2 (*right*), so that the vertical coordinate here (labeled ξ and measured from the center of mass of each filament) is approximately along the filaments. The solid line shows the column density-weighted ξ-velocity, averaged over the filament width. Its value is given by the upper horizontal scale. The global collapse of the filaments, with superimposed local collapses, is apparent.

umn density maps are shown in Fig. 4. Superposed on these maps, we show plots of the mean column density-weighted velocity perpendicular to the line-of-sight and approximately along the filament (the vertical velocity in the projection of Fig. 4). This rendering clearly shows the large scale collapse of the filament along its long dimension, signaled by the sharp transition (jump) from positive velocities in the lower region to negative velocities in the upper region. But in addition to this global collapse, smaller jumps in velocity associated to smaller-scale (in size and mass) centers of collapse are also observed. The collapsing regions move along the filament, as they follow the large scale filament collapse, and so the velocity jumps around these regions are superposed on the average infall velocity towards the larger-scale center of mass.

4.3. Accretion onto and from the filaments

As mentioned above, the filaments are not depleted in a single crossing time (along their long dimension) as they fall onto the local collapse centers (the clumps) within them because the filaments themselves are accreting material from their surroundings. This infall of material occurs at lower densities than that of the filaments, and so the infall and the dense filament might not be both observable with the same molecular species. Nevertheless, we report here the accretion structure in the hope that it can be ultimately compared with that of observed filaments.

Figure 5 shows a position-velocity diagram along Filament 2, integrating along the same line-of-sight as in Figure 4, for gas with density below and above $10^3\,\mathrm{cm}^{-3}$. The velocity in this case is along the line of sight (LOS), and denoted $v_{\rm los}$. While gas with lower density (grayscale, red in the online version) forms a continuous structure along the filament, denser gas (contours, green in the online version) breaks into four separate structures. One of those individual structures is a disk surrounding a collapse region near the center of the filament (at $\xi \approx 0.5\,\mathrm{pc}$), distinguishable by the larger spread in LOS velocity. Smaller collapse centers are also noticeable (at $\xi \approx -5.5, -3$, and $5\,\mathrm{pc}$). Interestingly, LOS-velocity jumps are generally observed in both the local and the large-scale clump-filament systems

As shown in Figure 3, the gas falls onto the fil-

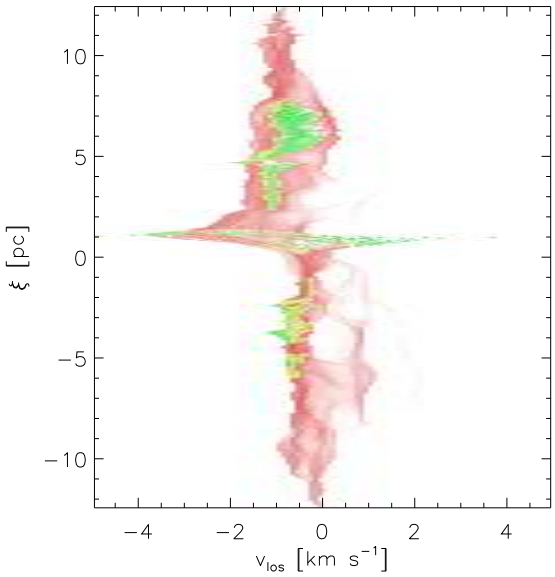

Fig. 5.— Position-velocity map along the center of the filament 2, integrated along the same direction as in fig. 4 so that the line-of-sight is approximately perpendicular to the filament and the ξ coordinate is measured along the filament. The red image corresponds to gas with $n < 10^3\,\mathrm{cm}^{-3}$, while the green image corresponds to denser gas. Both show the column density of gas per unit velocity interval (on a logarithmic scale) in the range $3\times10^{19} - 3\times10^{23}\,\mathrm{cm}^{-2}(\,\mathrm{km\ s}^{-1})^{-1}$. Most of the gas in both density regimes is clearly separated in velocity space, with only narrow regions of overlap (yellow). See the electronic edition of the Journal for a color version of this figure.

ament in an oblique direction, and gradually becomes a flow *along* the filament as one moves towards the filament's axis. That is, this change of direction happens as the gas density increases. Therefore, when considering the velocity component perpendicular to the filament ($v_{\rm los}$ in fig. 5), gas in diferent density regimes should separate in velocity space. This is noticeable in Figure 5 as a clear separation of the gas in these regimes (red and green images in the online version), with only a small superposition visible as a yellow area in the online version (with exception of the disk near the center, where the nature of the gas flow is different to the rest of the filament).

Figure 6 shows the projected accretion onto Filament 2, defined as the flux across a contour defined by a given column density value. Shown are both the flux across longitudinal contour segments (the flux perpendicular to the filament; filled circles) and across a contour segment perpendicular to the filament (the flux along the filament; plus signs). As mentioned above, the filament accretes gas mainly in the direction perpendicular to it. But, since the filament itself is falling onto the clump at the same time it is accreting, the inflow parallel to the filament, although small, is non-neglegible. For example, at a threshold density of $3 \times 10^{21}\,{\rm cm}^{-2}$, the flux along the filament is a factor of ~ 10 smaller than the perpendicular accretion. In the scenario pictured above, this should not be surprising: the filament flows along its long direction, but keeps being replenished by its envelope. So, at a surface defined solely by a column density value there will be flux due to both accretion (mainly perpendicular) onto the filament as well as flux (parallel) corresponding to infall due to the collapse of the filament as a whole.

The longitudinal accretion rate the filament becomes comparable to the perpendicular one at $N_{thr} \sim 2 \times 10^{22}\,{\rm cm}^{-2}$. This may be understood in terms of mass conservation, since the filament is not a hydrostatic structure, but rather, a flow feature, so that all the mass that accretes perpendicularly to the filament must eventually flow away in the longitudinal direction. Considering that the filament is $\sim 15\,{\rm pc}$ long, its total perpendicular accretion rate is $\sim 150 M_\odot\,{\rm Myr}^{-1}$.

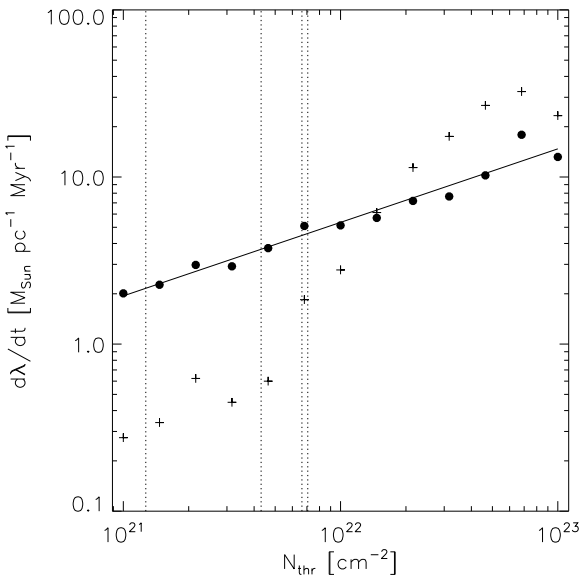

Fig. 6.— Accretion into the filament 2, defined as the mass flux across the contour containing the column density N_{thr} in the directions perpendicular (*dots*) and parallel (*crosses*) to the filament. Dotted vertical lines show column densities corresponding to radii $0.03, 0.1, 0.3$ and $1\,{\rm pc}$ (*right to left*), according to the fit to the column density profile discussed in §4.4. At $N > 10^{22}\,{\rm cm}^{-2}$, the filament's radius cannot be derived from the column density profile fit. The structures at column densities larger than these are isolated clumps, rather than part of the fitted filament radial column density profile. The perpendicular accretion may be fitted by ${\rm d}\lambda/{\rm d}t = 5.35 M_\odot\,{\rm pc}^{-1}\,{\rm Myr}^{-1}(N/10^{22}\,{\rm cm}^{-2})^{0.44}$ (*solid line*).

4.4. Filament profile

It has been suggested that filaments observed in molecular clouds might have a Plummer-like profile, in the direction perpendicular to the filament's long axis. Arzoumanian et al. (2011) explored a number of filaments observed with *Herschel* and fitted a profile with a core of constant density ρ_c and radius R_c, and a power-law envelope, described as

$$\rho_P(R) = \frac{\rho_c}{\left[1 + (R/R_c)^2\right]^{p/2}}, \qquad (1)$$

where R is the distance perpendicular to the filament's long axis, and p is the (negative) logarithmic slope of the density profile at large R. The corresponding column density perpendicular to the filament is (Arzoumanian et al. 2011)

$$\Sigma_P(R) = \frac{A_p \rho_c R_c}{\left[1 + (R/R_c)^2\right]^{(p-1)/2}}, \qquad (2)$$

where $A_p = \int_{-\infty}^{\infty} \mathrm{d}u/(1+u^2)^{p/2}$. They found that the filaments are well fitted for values of p in the range $1.5 < p < 2.5$, and a characteristic Gaussian FWHM of 0.1 pc, which corresponds to $R_c \approx 0.03$ pc.

To compare with their results, we again consider Filament 2, rotated as described above (§4.2). In order to distinguish the filament from nearby clumping, we have fitted a two-component column density model of the form of eq. (2) at each position ξ along the filament with peak column density $N > 2 \times 10^{21}\,\mathrm{cm}^{-2}$. We then considered the component with higher central column density as defining the center of the filament. Next, a mean column density profile perpendicular to the filament was calculated by averaging in azimuth and along the filament. Figure 7 shows the resulting mean profile. The best single-component fit has $R_c = 0.31$ pc, $\rho_c/m_{eff} = 3022\,\mathrm{cm}^{-3}$, and $p = 2.4$. This filament width is consistent with the filament data compiled by Myers (2009) for a number of nearby star-forming regions. We also added a constant column density term to the model in order to account for the low density diffuse gas present in the simulation that is not observable in molecular line emision, but the fitted parameters change only marginally. In both cases, the spread

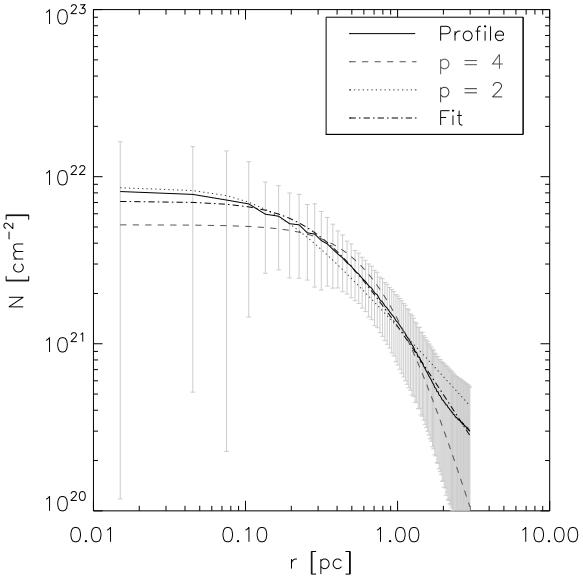

Fig. 7.— Mean column density profile for filament 2 (*solid line*), as a function of distance perpendicular to the filament. Error bars show the spread of column density profiles for different values of ξ. The best fit of the form of eq. 2 (*dot-dashed line*) is shown, along with fits with $p = 2, 4$ (*dotted and dashed lines*, respectively) for comparison.

in column density profiles along the filament is much larger than the error in the fit.

Figure 7 also shows the fitted profile for the $p = 4$ case, which corresponds to an isothermal cylinder in hydrostatic equilibrium (Ostriker 1964). With the apropriate parameters, a $p = 4$ model can be fitted within the large spread in column density values. However, departures from the average profile show trends (systematically below the mean profile in the constant core region, for example), suggesting a bad fit. Also, since the $p = 4$ model falls more rapidly than the mean profile, the fit is more sensitive to the constant column density term mentioned above (in fact, this is the only case where a non-neglegible column density base was returned by the fitting procedure). Regardless, a bad fit for a hydrostatic model should not be surprising given the dynamical nature of the filament in the simulation. In fact, Fig. 7 also shows a fit with $p = 2$, which Arzoumanian et al. (2011) used to fit one of their filaments. It is seen that this value of p provides a much better fit for our filament than the case $p = 4$, although the best fit is obtained for $p = 2.4$.

In contrast with observations, the numerical model yields the full spatial distribution of the gas, allowing us to explore the three dimensional structure of the filament. With this in mind, we repeated the above procedure but using a profile of the form of eq. (1) to fit the volume density distribution of the filament 2. In this case, the two-component fit was performed for each ξ-position along the filament with $n > 10^3\,\mathrm{cm}^{-3}$. Again, the main component is defined as that with larger central column density. Figure 8 shows the fitted parameters along the filament. The fitting procedure returns continuous positions for the center of the main component along the filament, suggesting that it is reasonably well defined by the fit. But it is noticeable that the distribution of centers of the secondary component, although not really continuous, tends to aglomerate to the right of the main component. This behavior is also present in the distribution of ρ_c and p-values along the filament. We envision two posible interpretations. One is that the filament is really a bundle of smaller filaments, as proposed by Hacar et al. (2013) for filaments in the Taurus region, that may be separated in velocity space. Another interpretation, which we find more plausible, is that the filament is not symmetric and so, using a symmetric form for the fit (either in real or in velocity space), artificially yields multiple, displaced components. This lack of symmetry is suggested by the skewed velocities in Figure 5.

With the center of the filament defined by the main component, we may average to obtain a (cylindrically symmetric) radial density profile characteristic of the filament (see fig. 9), which, following Arzoumanian et al. (2011), was then fitted by a single Plummer-like shape. In this case, the best single-component fit has parameters $R_c = 0.11\,\mathrm{pc}$, $\rho_c/m_{eff} = 8646\,\mathrm{cm}^{-3}$, and $p = 1.864$. This value of p implies a shallower volume density profile than the corresponding column density one. This is, however, to be expected, as the column density, seen in projection, increases towards the central axis of the filament due to the combined effects of a larger volume density at the central axis and of a longer integration path there. Nevertheless, without the smoothing effect provided by the line-of-sight integration, the spread in values in the volume density profiles is much larger than in the column density case, and therefore this fit is less reliable.

5. SUMMARY AND DISCUSSION

We performed SPH simulations of the formation of a molecular cloud from a convergent flow of diffuse gas. As in previous works, the resulting cloud is highly dynamic and, due to hydrodynamic and thermal instabilities, becoming turbulent and rapidly fragmenting into substructure. Nevertheless,, the "turbulent" motions are unable to stabilize the cloud and soon its dynamics becomes dominated by gravity, and the cloud begins to collapse. However, because the cloud continues o accrete, its mass continues to grow, and soon it contains a large number of Jeans masses (Vázquez-Semadeni et al. 2007). This naturally leads to the formation of filaments, since the multi-Jeans mass flow behaves similarly to a pressureless flow, which is known to collapse along its shortest dimension first (Lin et al. 1965), so that the initially planar cloud collapses onto filaments, which then collapse into clumps.

The filaments are not equilibrium structures at all, and instead are highly dynamical. They can be considered intermediate steps of the cloud's

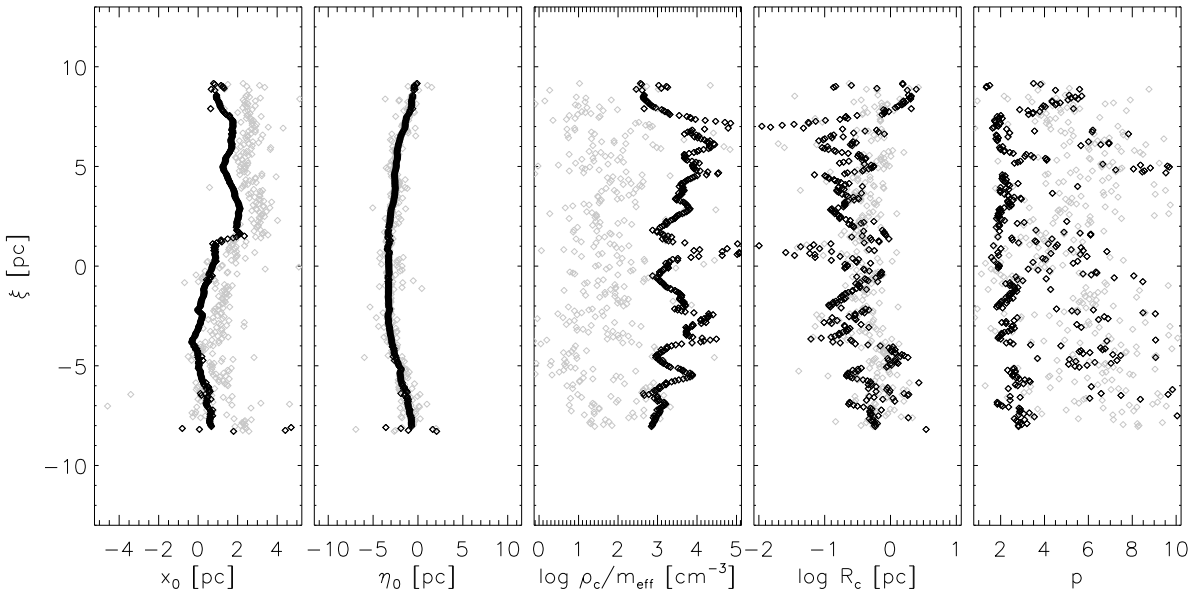

Fig. 8.— Resulting parameters when a two-component profile of the form of eq. (1) is fitted to Filament 2. x_0 and η_0 represent the coordinates of the center of the profile, with η being the direction parallel to the line-of-sight in fig. 4. Dark dots correspond to the main component of the fit, while light dots show the secondary component.

collapse, constituting channels through which the gas is funneled from the extended cloud onto the clumps. These filaments are the loci of colliding streams on the parent planar structures, where the flow gets reoriented and directed towards its final destination – the clumps within the filaments, which have conditions appropriate for star formation.

In our simulation, the gravitational collapse in the individual centers (modeled with sink particles), is not instantaneous but starts $\sim 20\,\mathrm{Myr}$ into the simulation and continues well after the filaments finish to accrete onto the clumps. Moreover, the filaments themselves are falling into the largest-scale potential well, generating new structures that eventually merge into each other, forming a larger-scale hub-filament system towards the end of the simulation.

The simulation presented here formed two prominent filaments, each with $\sim 600 M_\odot$ out to radii $\sim 0.3\,\mathrm{pc}$, and lengths $\sim 15\,\mathrm{pc}$, implying linear mass densities $\lambda \sim 40 M_\odot\,\mathrm{pc}^{-1}$. We furthermore studied the radial density and column density profiles of the filament, finding that the column density profile is reasonably well fitted by a Plummer-like profile, whose best-fit parameters are $R_c = 0.31\,\mathrm{pc}$ and $p = 2.4$. In turn, the three-dimensional radial density distribution was best fitted with $R_c = 0.1\,\mathrm{pc}$ and $p \approx 1.9$, although this fit was less certain because in the three-dimensional measurement no averaging along the LOS is made.

These values are qualitatively consistent with observational results. For example, André et al. (2010) find that their sample of filaments in the Aquila region have linear mass densities $\lambda > 15 M_\odot\,\mathrm{pc}^{-1}$, while Arzoumanian et al. (2011) find that their filaments typically have Plummer-type column density radial profiles with $R_c \sim 0.1\,\mathrm{pc}$ and $1.5 < p < 2.5$. However, while they speculate that their filaments may form as the result of the dissipation of large-scale turbulence, because their characteristic thickness is similar to that of the sonic scale, below which the "turbulence" becomes subsonic, in our case, the filaments are not a result of turbulence nor their thickness is the result of having dissipated the turbulence. Instead, they are an intermediate stage of the gravitational

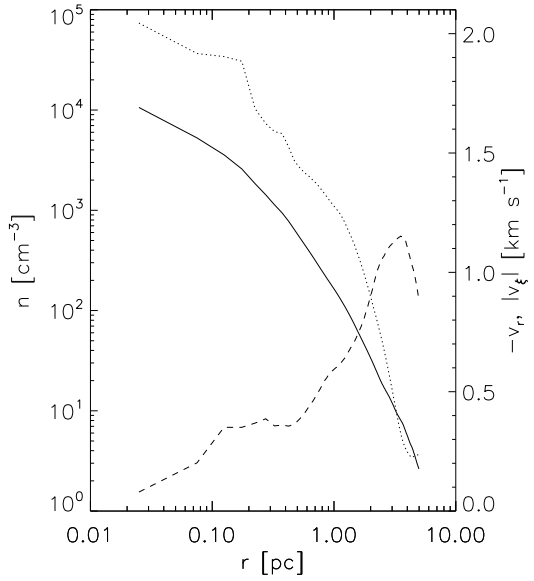

Fig. 9.— Azimuthally averaged density (*solid line*), radial infall velocity (*dashed*), and longitudinal velocity (*dotted*) for the filament 2. As gas is accreted onto the filament, its (radial) inflowing velocity gradually turns and the gas flows along the filament.

collapse, funneling gas to the local collapse centers – the clumps – and their thickness is the result of the reorientation of the flow from being mainly perpendicular to being mainly parallel to the filaments' axes.

We also measured the accretion rates perpendicular (onto) and parallel (along) the filament. The rates are not unique, but instead depend on the radial position along the filament. Because of the column density profile, this translates into a column density dependence of the accretion rates. We found that, as the column density varies from 10^{21} to $10^{23}\,\mathrm{cm}^{-2}$, the accretion rate linear density perpendicular to the filament (i.e., onto to it) ranges between 2 and 20 $M_\odot\,\mathrm{Myr}^{-1}\,\mathrm{pc}^{-1}$, while the linear accretion density from the filament onto the clump ranges between 0.3 and 30 $M_\odot\,\mathrm{Myr}^{-1}\,\mathrm{pc}^{-1}$. Considering that the filament is $\sim 15\,\mathrm{pc}$ long, its total perpendicular accretion rate is $\sim 150 M_\odot\,\mathrm{Myr}^{-1}$.

Our measured linear accretion rate densities, which peak at $2\text{–}3\times 10 M_\odot\,\mathrm{pc}^{-1}\,\mathrm{Myr}^{-1}$, are at least half an order of magnitude lower than those inferred by Schisano et al. (2013), although their estimate was an indirect one, assuming that the characteristic timescale for the process of moving the material along the filament is equal to that of the lifetime of the protostellar objects being formed in the clumps, $\sim 10^4$ yr. This is a rather uncertain assumption, which may overestimate the accretion rate estimate. On the other hand, our total measured accretion rate of $\sim 150 M_\odot\,\mathrm{Myr}^{-1}$ matches very well that inferred by Kirk et al. (2013) ($\sim 130 M_\odot\,\mathrm{Myr}^{-1}$). However, the filament they studied was at a much smaller (sub-pc) scale, and therefore the comparison may not be conclusive.

We conclude from our results that the process of hierarchical and chaotic gravitational fragmentation produces filaments that have physical conditions and accretion rates that are qualitatively similar to those found in recent observational studies, suggesting that this mechanism may indeed be responsible for their formation. However, more systematic studies need to be performed where the mass and size scales of the filaments in both the observations and simulations are better matched, in order to determine whether in this case their radial column density profiles and accretion rates match at the quantitative level. We plan to per-

form such a study in the near future.

This work has received financial support from UNAM-DGAPA PAPIIT grant IN111313 to GCG and CONACYT grant 102488 to EVS. The numerical simulation was performed on the cluster at our Center acquired through the latter grant.

REFERENCES

André P. et al., 2010, A&A, 518, L102

Arzoumanian D. et al., 2011, A&A, 529, L6

Audit, E., & Hennebelle, P. 2005, A&A, 433, 1

Bally, J., Lanber, W. D., Stark, A. A., & Wilson, R. W. 1987, ApJ, 312, L45

Balsara, D., Ward-Thompson, D., & Crutcher, R. M. 2001, MNRAS, 327, 715

Bate, M. R., Bonnell, I. A., & Price, N. M. 1995, MNRAS, 277, 362

Csengeri, T., Bontemps, S., Schneider, N., Motte, F., & Dib, S. 2011, A&A, 527, A135

Curry, C. L. 2000, ApJ, 541, 831

Elmegreen, B. G. 1987, ApJ, 312, 626

Federrath, C., Banerjee, R., Clark, P. C., & Klessen, R. S. 2010, ApJ, 713, 269

Feitzinger, J. V., Perschke, M., Haynes, R. F., Klein, U., & Wielebinski, R. 1987, Vistas in Astronomy, 30, 243

Field, G. B., Blackman, E. G., & Keto, E. R. 2008, MNRAS, 385, 181

Galván-Madrid, R., Keto, E., Zhang, Q., et al. 2009, ApJ, 706, 1036

Gehman, C. S., Adams, F. C., & Watkins, R. 1996, ApJ, 472, 673

Goldsmith, P. F., Heyer, M., Narayanan, G., et al. 2008, ApJ, 680, 428

Gómez G. C., Vázquez-Semadeni E., Shadmehri M., Ballesteros-Paredes J., 2007, ApJ, 669, 1042

Gutermuth, R. A., Bourke, T. L., Allen, L. E., et al. 2008, ApJ, 673, L151

Hacar, A., Tafalla, M., Kauffmann, J., & Kovács, A. 2013, A&A, 554, 55

Heiles, C., & Troland, T. H. 2003, ApJ, 586, 1067

Heitsch, F., Ballesteros-Paredes, J., & Hartmann, L. 2009, ApJ, 704, 1735

Heitsch, F., Burkert, A., Hartmann, L. W., Slyz, A. D., & Devriendt, J. E. G. 2005, ApJ, 633, L113

Heitsch, F., Slyz, A. D., Devriendt, J. E. G., Hartmann, L. W., & Burkert, A. 2006, ApJ, 648, 1052

Henning, T., Linz, H., Krause, O., et al. 2010, A&A, 518, L95

Hoyle, F. 1953, ApJ, 118, 513

Jappsen, A.-K., Klessen, R. S., Larson, R. B., Li, Y., & Mac Low, M.-M. 2005, A&A, 435, 611

Juvela, M., Pelkonen, V.-M., & Porceddu, S. 2009, A&A, 505, 663

Kim, W.-T., Ostriker, E. C., & Stone, J. M. 2002, ApJ, 581, 1080

Kirk, H., Myers, P. C., Bourke, T. L., et al. 2013, ApJ, 766, 115

Klein, R. I., & Woods, D. T. 1998, ApJ, 497, 777

Koyama, H., & Inutsuka, S.-i. 2002, ApJ, 564, L97

Larson, R. B. 1985, MNRAS, 214, 379

Lin, C. C., Mestel, L., & Shu, F. H. 1965, ApJ, 142, 1431

Men'shchikov, A., André, P., Didelon, P., et al. 2010, A&A, 518, L103

Miyama, S. M., Narita, S., & Hayashi, C. 1987, Progress of Theoretical Physics, 78, 1051

Molinari, S., Swinyard, B., Bally, J., et al. 2010, A&A, 518, L100

Myers P. C., 2009, ApJ, 700, 1609

Nagai, T., Inutsuka, S.-I., & Miyama, S. M. 1998, ApJ, 506, 306

Naranjo-Romero, R., Zapata, L. A., Vázquez-Semadeni, E., et al. 2012, ApJ, 757, 58

Ostriker J., 1964, ApJ, 140, 1056

Padoan, P., Juvela, M., Goodman, A. A., & Nordlund, Å. 2001, ApJ, 553, 227

Pavlovski, G., Smith, M. D., Mac Low, M.-M., & Rosen, A. 2002, MNRAS, 337, 477

Pon, A., Toalá, J. A., Johnstone, D., et al. 2012, ApJ, 756, 145

Schisano, E. 2013, submitted

Schneider, N., Csengeri, T., Bontemps, S., et al. 2010, A&A, 520, A49

Schneider, N., Csengeri, T., Hennemann, M., et al. 2012, A&A, 540, L11

Toalá J. A., Vázquez-Semadeni E., Gómez G. C., 2012, ApJ, 744, 190

Vazquez-Semadeni, E. 2012, in "Magnetic Fields in Diffuse Media", eds. E. de Gouveia dal Pino, A. Lazarian, in press (arXiv:1208.4132)

Vázquez-Semadeni, E., Banerjee, R., Gómez, G. C., et al. 2011, MNRAS, 414, 2511

Vázquez-Semadeni E., Colín P., Gómez G. C., Ballesteros-Paredes J., Watson A. W., 2010, ApJ, 715, 1302

Vázquez-Semadeni E., Gómez G. C., Jappsen A.-K., Ballesteros-Paredes J., González R. F., Klessen R. S., 2007, ApJ, 657, 870

Vázquez-Semadeni E., Gómez G. C., Jappsen A.-K., Ballesteros-Paredes J., Klessen R. S., 2009, ApJ, 707, 1023

Vázquez-Semadeni, E., Ryu, D., Passot, T., González, R. F., & Gazol, A. 2006, ApJ, 643, 245

Vishniac, E. T. 1994, ApJ, 428, 186

Walder, R., & Folini, D. 2000, Ap&SS, 274, 343

This 2-column preprint was prepared with the AAS LaTeX macros v5.2.